Soft Topological Metamaterials with Pronounced Polar Elasticity in Mechanical and Dynamic Behaviors

Maya Pishvar and Ryan L. Harne*

Department of Mechanical and Aerospace Engineering, The Ohio State University, Columbus, Ohio 43210, USA

(Received 12 June 2020; revised 11 August 2020; accepted 25 September 2020; published 20 October 2020)

We realize soft topological mechanical metamaterials with pronounced polar elastic responses (i.e., softer on one edge than the other) in both the quasistatic and dynamic regimes. Numerical simulations and experimental results confirm the presence of directional dependence in metamaterial response at low and high strain rates, despite the use of lossy elastomer as bulk media. The metamaterials exhibit means to tailor the location of topologically protected uniaxial mechanical stiffnesses by virtue of both loading orientation and geometric changes to the lattice architecture. High-speed video recordings show strong topologically protected asymmetric wave propagation for the soft metamaterials subjected to impact. The results indicate a class of metamaterial architectures possessing polar elastic behavior and confirm the persistence of the response in lossy media.

DOI: 10.1103/PhysRevApplied.14.044034

I. INTRODUCTION

The Maxwell-Betti reciprocal theorem for linear systems states that forces exerted at point X resulting in displacements at point Y produce the same displacements at point X when the forces are applied at point Y [1–3]. Nonreciprocity therefore breaks such symmetry of system behavior by eliminating the correspondence of transfer between displacements and forces [4]. The symmetry of linear elasticity may also be broken by the existence of polar elasticity. Polar elasticity is manifested by differing stiffnesses at opposite edges, so that collocated force and displacement ratios are distinct at opposite material edges [5]. The ability to break spatial symmetries in mechanical responses in soft matter would open exciting frontiers in numerous scientific disciplines and applications [6–11]. Recently, nonreciprocity in mechanical properties is cultivated in mechanical metamaterials by leveraging nonlinearities with geometrical asymmetries or by tailoring topological features of the material frame [12,13]. The topology of a pyrochlore lattice metamaterial has also been found to induce polar elastic behavior when subjected to compressive forces [5].

Polar and nonreciprocal elastic behavior in the dynamic regime is widely considered as a means to create mechanical diodes, lattices with limited wave backscattering, and structures exhibiting asymmetric wave propagation [14–16]. The underlying mechanisms that produce such asymmetries are the topologically protected floppy modes on edges or interfaces borne out of metamaterial microstructure [4,17,18]. Topological floppy modes are analogs of protected electronic boundary modes in the quantum Hall effect and in topological insulators [19–21]. Kane and Lubensky [17] identified the presence of such boundary modes in Maxwell lattices [22], for which the average number of constraints equals the number of degrees of freedom. Square and kagome architectures are examples of Maxwell lattices [23]. With small changes in the lattice geometry, topological polarization is induced. As such, floppy modes reside along edges or are manifested as plane-wave-like states in the bulk [17,24]. In addition, uniform twisting of a kagome lattice unit cell transforms topological polarization leading to contrasting edge stiffnesses and spatial localization of floppy edge modes [25]. Topologically protected edge modes therefore have been recently harnessed to cultivate non-natural dynamic behaviors in mechanical metamaterials [14,26–28] such as asymmetric wave transport [29]. These principles have also been integrated into foldable structures that exhibit directionally dependent bending stiffnesses [17,30,31].

In this work, we examine the manifestation of polar elasticity in mechanical and dynamic behaviors in topological metamaterials formulated with soft-matter-based lattices. We use simulations and experiments to characterize distinctive material responses observed when stress is applied at infinitesimal and finite rates and at various incidences to edges of such soft mechanical metamaterials. Our comprehensive assessment reveals means to govern directional dependence in transmission of stress through design and transformations of the soft elastic lattice. To build from the recent acceleration of interest in

*ryanharne@psu.edu

soft mechanical metamaterials [32–35], this work illuminates the origins and existence of polar elastic responses in the quasistatic and dynamic regimes of elastomeric topological lattices governed by stress application and lattice microstructure.

II. POLAR ELASTIC QUASISTATIC RESPONSES

The soft metamaterials investigated in this work are derived from a kagome lattice composed of 12 rows and 12 columns of unit cells (12 × 12). The samples are fabricated from Shore 15A durometer silicone rubber (Smooth-On Mold Star 15S, Macungie, PA). Figure 1 shows four fabricated metamaterial unit cells with varying deviations to an underlying unit cell cross section. To illustrate the difference between regular and topological lattice networks, we investigate four types of lattices. In sample S1, the regular kagome lattice employs two equilateral triangles in the unit cell. In sample S2, a topological deformed kagome lattice incorporates unit cells with one equilateral and one scalene triangle that are not relatively rotated. Sample S2 therefore deviates from sample S1 by the relative difference in cross section of one unit cell triangle. By contrast, "twist" or rotation of the unit cell triangles is incorporated into lattice samples S3 and S4. For metamaterial samples S3 and S4, the adjacent unit cell triangles are rotated by 26° and 48°, respectively, as observed in Fig. 1. Complete metamaterial design and fabrication details are given in Sec. 1.1 of the Supplemental Material [36].

Measurements of uniaxial mechanical properties of the metamaterials are conducted in a load frame (ADMET eXpert 5600), details of which can be found in Sec. 1.2 of the Supplemental Material [36]. Each sample is placed on an inclined plane with an angle of inclination equal to the lattice structure inclination angle, as illustrated in Fig. 2(a). Given the metamaterial geometries considered in this work, the inclination angles of planes supporting samples in mechanical property characterizations are 0°, 0°, 13°, and 24°, respectively, for samples S1, S2, S3, and S4. Vertical compressive displacements are applied to the samples using an indenter with triangular recess fitting the shape of the central triangular unit cell element of each sample. When the force and applied displacement are delivered down on the top edge of the lattice respecting the unit cell configurations in Fig. 1, here we term this the "Down Force" condition. The "Up Force" mechanical

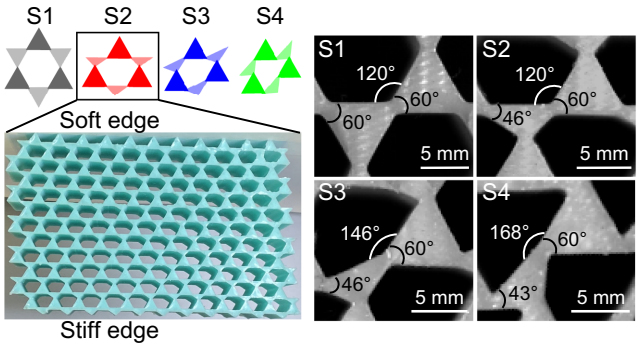

FIG. 1. Schematics and geometrical parameters of the unit cells for metamaterial samples S1, S2, S3, and S4. S1 is derived from a regular kagome lattice, while S2 is created from a topological deformed kagome lattice, leading to asymmetric stiffnesses along opposite edges of S2. By rotation of the unit cell triangles, a twist is introduced to the deformed kagome metamaterials S3 and S4.

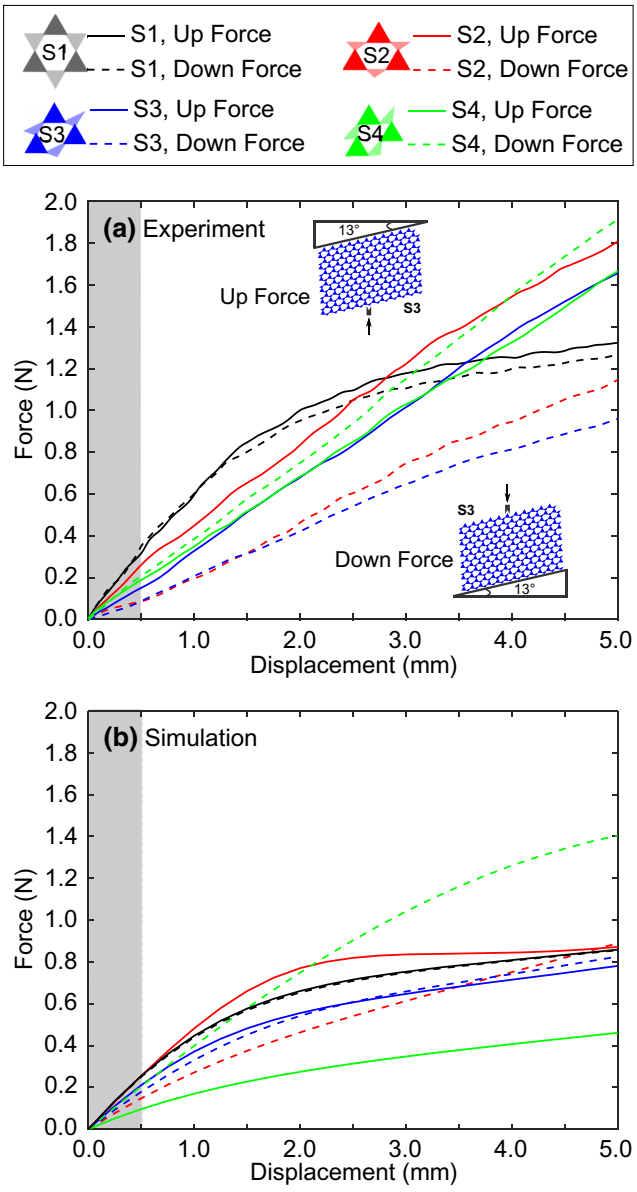

FIG. 2. (a) Measured and (b) simulated mechanical response of metamaterial samples S1, S2, S3, and S4 subjected to vertical compression in the upward (solid curves) and downward (dashed curves) directions. Samples S2, S3, and S4 demonstrate polar elastic behavior governed by the unit cell topology.

response is evaluated following rotation of the sample by 180° to characterize the mechanical properties of the bottom edge of the lattice. The uniaxial mechanical properties in Fig. 2 show that for uniaxial compression up to around 0.5 mm the samples respond linearly, highlighted by the shaded area in Fig. 2(a). The slope of a line linearly fitted to the measured properties in this regime corresponds to the uniaxial mechanical stiffness of the metamaterial sample. The stiffness values are tabulated in Table S2 within the Supplemental Material [36].

For the regular kagome metamaterial sample S1, the uniaxial mechanical stiffness measured from opposite edges is nearly identical in the linear regime, seen by the slopes of the solid and dashed black curves in Fig. 2(a). Yet, for the deformed kagome metamaterial samples S2, S3, and S4, Fig. 2(a) shows that the forces against the top edges are distinct from forces acting against the bottom edges when subjected to the same applied displacements. This serves as evidence of strong asymmetric mechanical stiffnesses in the linear regime. The existence of such behavior was suggested theoretically by Rocklin et al. [25].

In this work, the ratio between mechanical stiffnesses on the top and bottom edges (equivalently the ratio of Down Force stiffness to Up Force stiffness) is termed the polar elasticity coefficient (PEC). Thus, $\mathrm{PEC} \neq 1$ refers to broken symmetry in mechanical response, whereas $\mathrm{PEC} < 1$ indicates the top edge is softer than the bottom edge and vice versa for $\mathrm{PEC} > 1$. For the regular kagome metamaterial sample S1, the coefficient is $\mathrm{PEC}_{S1} = 1$, indicating symmetric mechanical behavior. For the sample S2 deformed kagome metamaterial, the polar elasticity coefficient is $\mathrm{PEC}_{S2} = 0.38$, confirming that the top edge is floppy (soft). Yet, by introducing the twist to the deformed kagome metamaterial samples S3 and S4, the polar elasticity coefficients are $\mathrm{PEC}_{S3} = 0.52$ and $\mathrm{PEC}_{S4} = 1.08$, respectively. This reveals that for sample S3 the top edge is floppy while for sample S4 the bottom edge is floppy. Thus, translations and rotations of an underlying unit cell design result in drastic asymmetry in mechanical properties by altering the topological states of the metamaterials. As a result, polar elastic response is strongest in the deformed kagome metamaterial without twist (sample S2) via the largest deviation from symmetric response, for which $\mathrm{PEC} = 1$, whereas the introduction of the unit cell twist in samples S3 and S4 may lead to reversed polarity of mechanical stiffness.

To gain a deeper understanding of the mechanisms governing this polar elastic phenomenon, we perform numerical simulations using the finite element method with COMSOL Multiphysics. We consider boundary and loading conditions that correspond to the experiments and assess the simulated mechanical behavior similar to the experimental characterizations. Full modeling details and comparison between experimental and simulation results are given in Secs. 1.3 and 2 of the Supplemental Material [36]. In the linear region, the regular kagome metamaterial sample S1 exhibits symmetric mechanical stiffness while asymmetric stiffnesses are found for deformed metamaterials S2, S3, and S4 in Fig. 2(b). Specifically, both simulations and experiments present that samples S2 and S3 are softer on the top edge than the bottom edge and sample S4 is stiffer on the top edge than the bottom edge (see Fig. 2). The similarity of the quantitative and qualitative trends of mechanical behavior between simulations and experiments verifies the model development. Marginal discrepancies between the measurements and model predictions may be due to (i) the boundary conditions in the experiments that may permit minor lateral motion of samples on the bottom inclined planes and (ii) manufacturing imperfections that may inhibit perfectly uniform ligament thicknesses in all unit cells of a given sample. Yet, the overall agreement of salient trends is sufficient justification to further explore the model to help uncover mechanisms governing onset of asymmetry in mechanical behavior.

III. APPROACHES TO TAILOR POLAR ELASTIC BEHAVIOR

We explore approaches to tailor the polar elastic response of the soft mechanical metamaterials. We define the oblique angle θ as the angle of incidence of applied displacement respecting the vertical (or normal) displacement application. Thus, both axial (normal) and tangential (shear) stresses are imparted upon the metamaterial samples, coupling axial and bending deformations at the lattice structure level. Figure 3(a) assesses the resulting PECs of the metamaterial samples S1, S2, S3, and S4 as functions of the oblique angle θ (see Sec. 2 of the Supplemental Material [36]). The regular kagome metamaterial sample S1 leads to $\mathrm{PEC}_{S1} \approx 1$ for all oblique angles of applied displacement, seen by the black circle data points in Fig. 3(a). On the other hand, for the deformed kagome metamaterials the topology of the unit cell governs an oblique angle where greatest and least polar elastic behavior is observed. For instance, in the deformed kagome metamaterial without twist sample S2, the PEC_{S2} ranges from 0.44 to 0.64, with the greatest polar elasticity in mechanical behavior at $\theta = 65°$. This indicates that regardless of the oblique angle, the bottom edge of metamaterial S2 is stiff while the top edge is soft so that the asymmetric stiffness is topologically protected. In deformed kagome metamaterials with twist, the polar elasticity coefficient varies according to $0.39 \leq \mathrm{PEC}_{S3} \leq 0.99$ and $0.37 \leq \mathrm{PEC}_{S4} \leq 2.39$, as depicted in Fig. 3(a) for samples S3 and S4, respectively. Thus, for sample S3 the metamaterial unit cell geometry supports topologically protected asymmetric mechanical behavior, and in fact greater stiffness variation than S2. Yet, for metamaterial sample S4, the floppy edges shift between top and bottom edges of the sample. Namely, for applied displacement normal to the edge, $\theta = 0°$, the top edge is 2.4

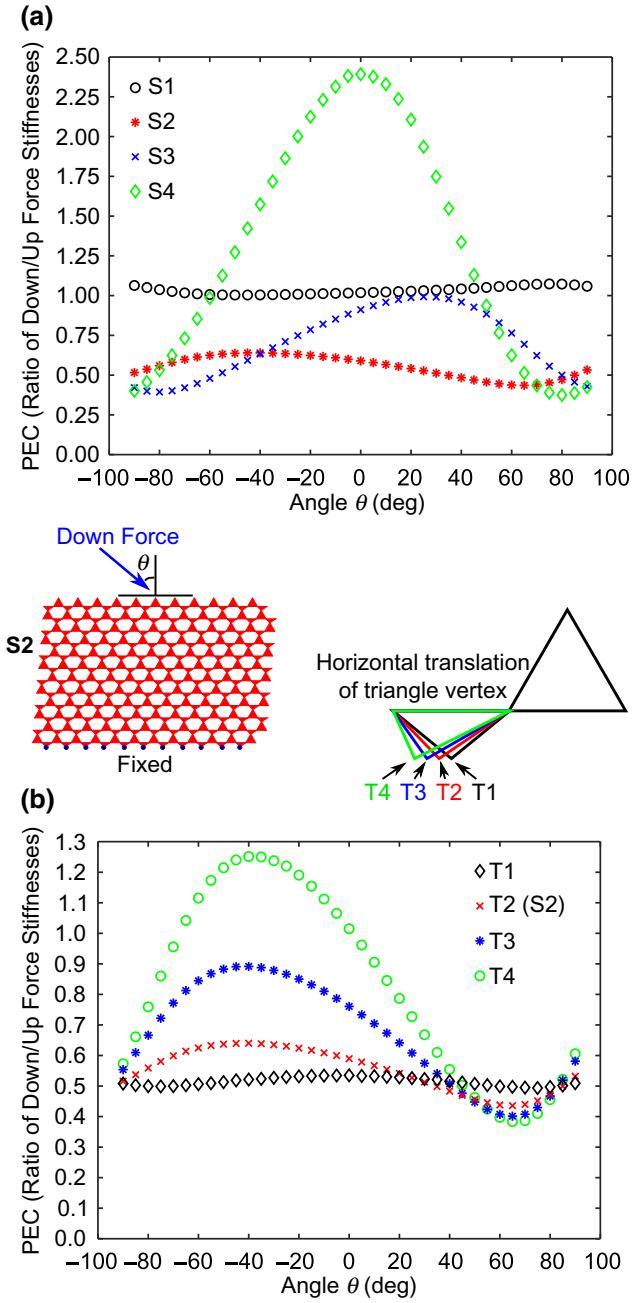

FIG. 3. Simulation of PEC as a function of oblique angle θ for (a) regular (S1), deformed (S2), and twisted deformed (S3 and S4) kagome lattice metamaterials, and for (b) deformed kagome lattices with relative translations for the vertex of a unit cell triangle. See the center schematic for naming convention of unit cells T1, T2, T3, and T4 according to changes in the unit cell geometry. PEC = 1 refers to symmetry, while PEC < 1 indicates the top edge is softer than the bottom edge and vice versa for PEC > 1.

times stiffer than the bottom edge ($PEC_{S4} = 2.39$), while at applied displacements inclined by $\theta = 80°$, the bottom edge is 2.7 times stiffer than the top edge ($PEC_{S4} = 0.37$). Moreover, sample S4 may also exhibit symmetric elastic behavior when the applied displacement is incident to the metamaterial surface at an angle of $\theta = -50°$ or $+45°$, indicating a broad range of elastic response associated with the topological polarization and angular incidence of mechanical load.

These trends suggest that the directional dependence in stiffness exhibits large sensitivity to twist or rotation of the adjacent unit cell triangles. To assess whether this characteristic extends to unit cell dimensional changes, we investigate the effects on PEC caused by relative translations for the vertex of a unit cell triangle in the deformed kagome metamaterials. A schematic representation of the enlarged unit cells along with the naming convention used for the unit cells is illustrated in the center of Fig. 3. For metamaterial sample T1, one equilateral triangle and one isosceles triangle form the unit cell. While for samples T2, T3, and T4 the vertex of the second triangle is horizontally translated by 0.66, 1.32, and 1.98 mm, respectively. Sample T2 is identical to sample S2 used in the prior investigation. Figure 3(b) depicts simulation results of the PEC as a function of oblique angle θ of the metamaterials having 12×12 unit cells. For sample T1, the triangles are symmetric, which results in a nearly constant polar elasticity coefficient of $PEC_{T1} \approx 0.5$. This indicates that the angle of incident applied stress or displacement does not cause a shift or change in the relative floppy and stiff nature of the edges. Yet, as the vertex of the unit cell triangle is translated by increasing distances from symmetry, the range of PEC increases. As a result, the polar elasticity coefficients for samples T2, T3, and T4 range according to $0.44 \leq PEC_{T2} \leq 0.64$, $0.40 \leq PEC_{T3} \leq 0.89$, and $0.38 \leq PEC_{T4} \leq 1.25$. Thus, the metamaterial sample T4 exhibits the greatest means to tailor polar elasticity in mechanical behavior and, like sample S4, permits a transformation of the location of the relative floppy and stiff edges. Ultimately, these findings demonstrate that the deformed kagome lattices have strong asymmetric stiffness capability, which can be markedly influenced by modifications in lattice unit cells and changes of orientation of force acting on metamaterials.

IV. DYNAMIC RESPONSE OF POLAR ELASTIC SOFT MATTER

Compelling examples of asymmetric wave transport in a kagome lattice metamaterial composed of thermoplastic acrylonitrile butadiene styrene recently emerged in Ref. [29]. Yet, the dissipation and diffusion of waves in soft, thermoset-based topological metamaterials have yet to be characterized for the impact of cross-linked elastomer on the passage of asymmetric waves. Recently, Vuyk and Harne [37] demonstrated the use of digital image correlation (DIC) to examine high-rate local deformation in elastomeric materials subjected to impact. Here, we employ high-speed video recordings (Photron FastCam SA-X2) of impact events on the soft mechanical metamaterials

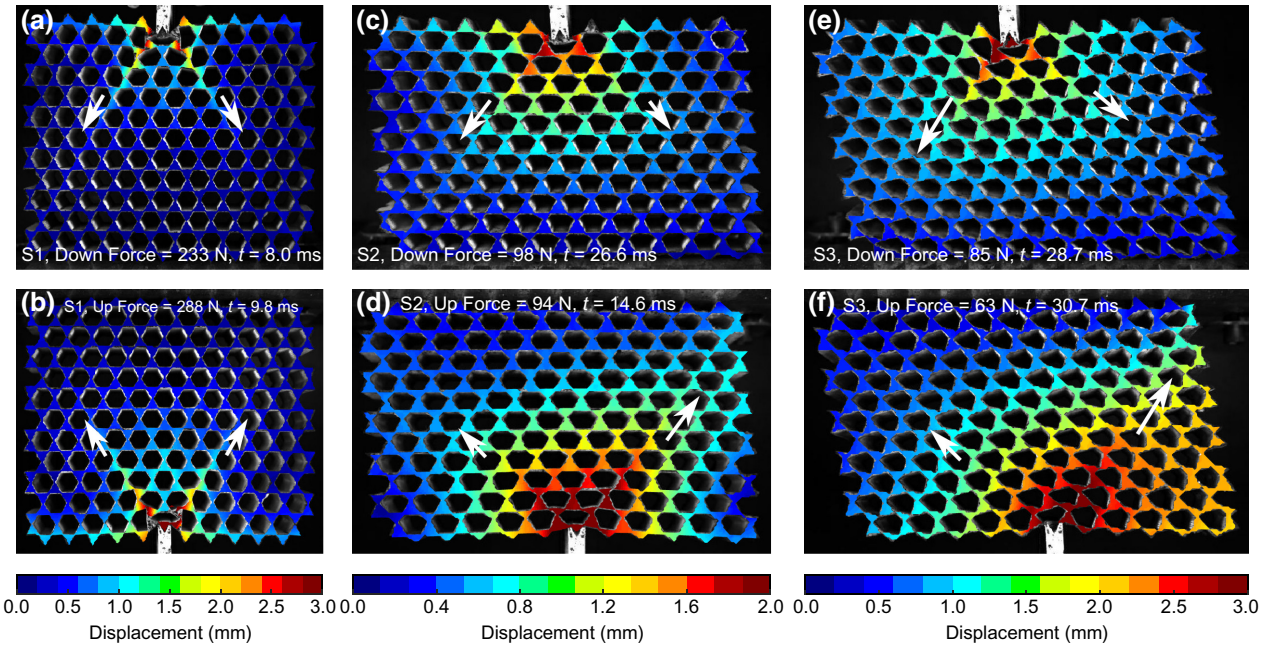

FIG. 4. Displacement magnitude measurements for metamaterial samples S1, S2, and S3 subjected to impact loading from opposite edges, displaying asymmetric wave propagation in the topological samples S2 and S3 and symmetric wave propagation in the regular sample S1. In (a), (c), and (e), impact is imparted to the top edge of S1, S2, and S3, respectively. On the other hand, in (b), (d), and (f), samples S1, S2, and S3 are struck from the bottom edge, respectively. White arrows illustrate the wave propagation directions and magnitudes along the lattice network.

with two-dimensional DIC to investigate the propagation of elastic waves. An edge of each metamaterial sample is struck by an impact hammer (PCB 086C03, Depew, NY) with an indenter shaped identical to the probe used for characterization of mechanical properties. The process is repeated for impact on the opposite edge after rotating the sample by 180°. The dynamic characterization is performed for samples S1, S2, and S3, to respectively illuminate the influences of topological protection (comparing regular sample S1 to topologically protected samples S2 and S3) and influences of unit cell twist (comparing sample S2 without and sample S3 with twist). The details of the experimental setup and videos of DIC data are presented in Secs. 1.4 and 3 of the Supplemental Material [36].

Figure 4 displays snapshots of displacement magnitudes for metamaterial samples S1, S2, and S3 subjected to impact loading from opposite edges. We observe mechanical waves that propagate at angles distinguished by the unit cell geometry of the metamaterial sample. The wave propagation directions and magnitudes along the lattice network are illustrated by white arrows in Fig. 4. Due to the viscoelastic dissipative nature of elastomeric metamaterials, propagating waves attenuate inside the metamaterial, leading to a strong gradient of the displacement magnitude unlike in thermoplastic based topological metamaterials [29]. Interestingly, the propagation of waves in the metamaterials studied here significantly depends on lattice topology, leading to gradations of symmetric or asymmetric energy transport. For the regular kagome metamaterial sample S1, a symmetric wave front is induced [Figs. 4(a) and 4(b)]. In the topological metamaterial samples S2 and S3, the wave propagation is evidently asymmetric. In addition, based on which edge is subjected to the impact, the transfer of energy differs significantly. For samples S2 and S3, impacts imparted to the top (or floppy) edge result in weak propagation of the mechanical energy towards the left according to the orientations in Figs. 4(c) and 4(e). On the other hand, if struck from the bottom (or stiff) edge with an upward-directed force, the waves propagate further into the bulk and to the right [Figs. 4(d) and 4(f)]. Metamaterial S3 exemplifies the greatest such asymmetric dynamic response. This confirms the direction dependence of shock mitigation behavior of the soft, elastomeric topological metamaterials studied here. Because topological properties are robust to small perturbations, the asymmetric wave propagation response of the metamaterial samples S2 and S3 is expected to be robust against imperfections such as imperfect sample molding, inevitable by the casting process. To further corroborate our conclusions, we report experimental results for a broader range of impact forces in the Supplemental Material [36].

V. CONCLUSIONS

In summary, we demonstrate pronounced polar elastic responses (softer on one edge than the other) in both the quasistatic and dynamic regimes in soft topological

metamaterials. The asymmetric uniaxial stiffness is found to be induced by a combination of unit cell microstructure and mechanical loading conditions. A particularly unique behavior is discovered as a reversal of elastic polarity as loading incidence changes, so long as the twist of adjacent unit cell geometries is sufficiently great. Strong asymmetric wave propagation is likewise revealed, giving evidence of direction dependence of shock mitigation behavior even in the presence of wave dissipation in soft elastomeric microstructure. The outcomes of this study motivate further investigation of the robustness of these behaviors despite the lossy nature of the elastomeric material and despite the potential for defects and precise imperfections, thus shedding light on topological metamaterials that may find future use as protective materials and structures.

ACKNOWLEDGMENTS

The authors acknowledge the support by the National Science Foundation Faculty Early Career Development Award (No. 1749699).

[1] S. W. Cheong, D. Talbayev, V. Kiryukhin, and A. Saxena, Broken symmetries, non-reciprocity, and multiferroicity, npj Quantum Mater. **3**, 1 (2018).
[2] E. M. McMillan, Violation of the reciprocity theorem in linear passive electromechanical systems, J. Acoust. Soc. Am. **18**, 344 (1946).
[3] M. Brandenbourger, X. Locsin, E. Lerner, and C. Coulais, Non-reciprocal robotic metamaterials, Nat. Commun. **10**, 1 (2019).
[4] S. D. Huber, Topological mechanics, Nat. Phys. **12**, 621 (2016).
[5] O. R. Bilal, R. Süsstrunk, C. Daraio, and S. D. Huber, Intrinsically polar elastic metamaterials, Adv. Mater. **29**, 1700540 (2017).
[6] D. Rus and M. T. Tolley, Design, fabrication and control of soft robots, Nature **521**, 467 (2015).
[7] F. Ilievski, A. D. Mazzeo, R. F. Shepherd, X. Chen, and G. M. Whitesides, Soft robotics for chemists, Angew. Chem., Int. Ed. **50**, 1890 (2011).
[8] N. W. Bartlett, M. T. Tolley, J. T. B. Overvelde, J. C. Weaver, B. Mosadegh, K. Bertoldi, G. M. Whitesides, and R. J. Wood, A 3D-printed, functionally graded soft robot powered by combustion, Science **349**, 161 (2015).
[9] B. C. K. Tee and J. Ouyang, Soft electronically functional polymeric composite materials for a flexible and stretchable digital future, Adv. Mater. **30**, 1802560 (2018).
[10] E. J. Markvicka, M. D. Bartlett, X. Huang, and C. Majidi, An autonomously electrically self-healing liquid metal-elastomer composite for robust soft-matter robotics and electronics, Nat. Mater. **17**, 618 (2018).
[11] S. L. Yeh and R. L. Harne, Structurally-integrated resonators for broadband panel vibration suppression, Smart Mater. Struct. in press (2020).
[12] C. Coulais, D. Sounas, and A. Alù, Static non-reciprocity in mechanical metamaterials, Nature **542**, 461 (2017).
[13] D. T. Ho, H. S. Park, and S. Y. Kim, Intrinsic rippling enhances static non-reciprocity in a graphene metamaterial, Nanoscale **10**, 1207 (2018).
[14] S. H. Mousavi, A. B. Khanikaev, and Z. Wang, Topologically protected elastic waves in phononic metamaterials, Nat. Commun. **6**, 8682 (2015).
[15] S. Li, D. Zhao, H. Niu, X. Zhu, and J. Zang, Observation of elastic topological states in soft materials, Nat. Commun. **9**, 1370 (2018).
[16] H. Nassar, B. Yousefzadeh, R. Fleury, M. Ruzzene, A. Alù, C. Daraio, A. N. Norris, G. Huang, and M. R. Haberman, Nonreciprocity in acoustic and elastic materials, Nat. Rev. Mater. **5**, 1 (2020).
[17] C. L. Kane and T. C. Lubensky, Topological boundary modes in isostatic lattices, Nat. Phys. **10**, 39 (2014).
[18] X. Mao and T. C. Lubensky, Maxwell lattices and topological mechanics, Annu. Rev. Condens. Matter Phys. **9**, 413 (2018).
[19] F. D. M. Haldane, Model for a Quantum Hall Effect Without Landau Levels: Condensed-Matter Realization of the "Parity Anomaly", Phys. Rev. Lett. **61**, 2015 (1988).
[20] M. Z. Hasan and C. L. Kane, Colloquium: Topological insulators, Rev. Mod. Phys. **82**, 3045 (2010).
[21] X. L. Qi and S. C. Zhang, Topological insulators and superconductors, Rev. Mod. Phys. **83**, 1057 (2011).
[22] J. C. Maxwell, L. On the calculation of the equilibrium and stiffness of frames, Philos. Mag. **27**, 294 (1864).
[23] K. Sun, A. Souslov, X. Mao, and T. C. Lubensky, Surface phonons, elastic response, and conformal invariance in twisted kagome lattices, Proc. Natl. Acad. Sci. U. S. A. **109**, 12369 (2012).
[24] J. Paulose, B. G. G. Chen, and V. Vitelli, Topological modes bound to dislocations in mechanical metamaterials, Nat. Phys. **11**, 153 (2015).
[25] D. Z. Rocklin, S. Zhou, K. Sun, and X. Mao, Transformable topological mechanical metamaterials, Nat. Commun. **8**, 14201 (2017).
[26] P. Wang, L. Lu, and K. Bertoldi, Topological Phononic Crystals with one-way Elastic Edge Waves, Phys. Rev. Lett. **115**, 104302 (2015).
[27] T. W. Liu and F. Semperlotti, Tunable Acoustic Valley–Hall Edge States in Reconfigurable Phononic Elastic Waveguides, Phys. Rev. Appl. **9**, 014001 (2018).
[28] Y. Guo, T. Dekorsy, and M. Hettich, Topological guiding of elastic waves in phononic metamaterials based on 2D pentamode structures, Sci. Rep. **7**, 18043 (2017).
[29] J. Ma, D. Zhou, K. Sun, X. Mao, and S. Gonella, Edge Modes and Asymmetric Wave Transport in Topological Lattices: Experimental Characterization at Finite Frequencies, Phys. Rev. Lett. **121**, 094301 (2018).
[30] B. G. G. Chen, N. Upadhyaya, and V. Vitelli, Nonlinear conduction via solitons in a topological mechanical insulator, Proc. Natl. Acad. Sci. U. S. A. **111**, 13004 (2014).
[31] B. G. G. Chen, B. Liu, A. A. Evans, J. Paulose, I. Cohen, V. Vitelli, and C. D. Santangelo, Topological Mechanics of Origami and Kirigami, Phys. Rev. Lett. **116**, 135501 (2016).

[32] K. Bertoldi, V. Vitelli, J. Christensen, and M. van Hecke, Flexible mechanical metamaterials, Nat. Rev. Mater. **2**, 1 (2017).
[33] C. Coulais, E. Teomy, K. de Reus, Y. Shokef, and M. van Hecke, Combinatorial design of textured mechanical metamaterials, Nature **535**, 529 (2016).
[34] B. Florijn, C. Coulais, and M. van Hecke, Programmable Mechanical Metamaterials, Phys. Rev. Lett. 113, 175503 (2014).
[35] C. Coulais, J. T. B. Overvelde, L. A. Lubbers, K. Bertoldi, and M. van Hecke, Discontinuous Buckling of Wide Beams and Metabeams, Phys. Rev. Lett. **115**, 044301 (2015).
[36] See Supplemental Material at http://link.aps.org/supplemental/10.1103/PhysRevApplied.14.044034 for a description of the experiments, details of finite-element modeling, and further discussion on supporting modeling results and movies.
[37] P. Vuyk and R. L. Harne, Collapse characterization and shock mitigation by elastomeric metastructures, Extreme Mech. Lett. **37**, 100682 (2020).
[38] S. Cui and R. L. Harne, Characterizing the nonlinear response of elastomeric material systems under critical point constraints, Int. J. Solids Struct. **135**, 197 (2018).
[39] D. Solav, K. M. Moerman, A. M. Jaeger, K. Genovese, and H. M. Herr, MultiDIC: An open-source toolbox for multi-view 3D digital image correlation, IEEE Access **6**, 30520 (2018).

Supplemental Material: Soft topological metamaterials with pronounced polar elasticity in mechanical and dynamic behaviors

Maya Pishvar and Ryan L. Harne*

Department of Mechanical and Aerospace Engineering, The Ohio State University, Columbus, OH 43210, USA

** Correspondence to: harne.3@osu.edu*

1 Experimental and modeling details

1.1 Metamaterial fabrication process

The metamaterial samples are fabricated by casting 15A Durometer silicone rubber (Smooth-On Mold Star 15S) in 3D-printed (FlashForge Creator Pro) acrylonitrile butadiene styrene (ABS) molds having negative shapes of the desired geometries. The depth of metamaterial cross-sections is 33.00 mm, which is the same depth as the constant cross-section molds. After curing at room temperature, the samples are demolded. The geometric notations of the metamaterial samples are shown in Figure S1. As can be seen in Figure S1, two adjacent triangles form an underlying kagome lattice. To generate the cross-section geometry of the metamaterial, an offset dimension from the triangles is used. The offset dimension t is the distance away from the nominal unit cell triangles that the material extends. Thus, the ligaments of material that interface adjacent triangles in the metamaterials are approximately $2t$ in thickness. The design parameters are listed in Table S1.

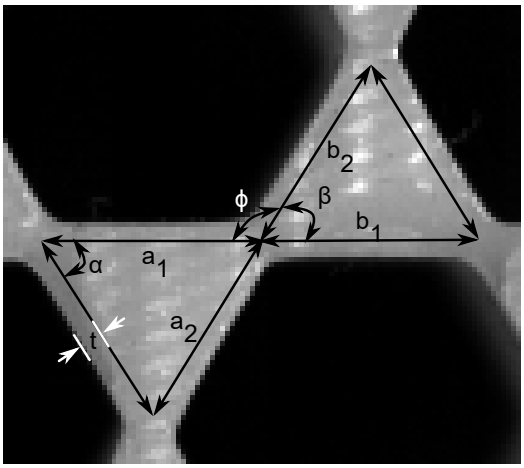

Figure S1. Geometric notations of the metamaterial samples.

Table S1. Geometric parameters of the unit cells for metamaterial samples S1, S2, S3, and S4.

Sample	a_1 (mm)	a_2 (mm)	b_1 (mm)	b_2 (mm)	t (mm)	α (degrees)	β (degrees)	ϕ (degrees)
S1	6.00	6.00	6.00	6.00	0.20	60	60	120

S2	6.00	4.38	6.00	6.00	0.20	46	60	120
S3	6.00	4.41	6.00	6.00	0.20	46	60	146
S4	6.00	4.17	6.00	6.00	0.20	43	60	168

1.2 Characterization of mechanical properties

Mechanical properties of the metamaterials are characterized by uniaxial compression experiments performed using a load frame (ADMET eXpert 5600 load frame, PCB 1102-05A load cell, Micro-Epsilon ILD 1700-200 laser displacement sensor) at a crosshead speed of 0.5 mm/min. The experimental set-up is shown in Figure S2. Because of the lattice geometries, it is necessary to test samples S3 and S4 on an inclined plane, with angle of inclination that matches the lattice structure inclination. Accordingly, samples S3 and S4 are placed on 3D-printed inclined planes with angles of 13º and 24º, respectively. It is noted that samples S3 and S4 could alternatively be cut so that the top surface remains horizontal, although this technique requires that different samples are needed for Down and Up Force characterizations. Samples S1 and S2 are evaluated in the load frame on a flat plate since there are no rotations between unit cell constituents in the geometries for S1 and S2. During the experiments, a uniaxial compressive "Down" directed force is applied with a 3D-printed triangle-shaped indenter that interfaces with a top center edge triangle of metamaterial sample through the whole triangle cross-section. The metamaterial is rotated 180° in order to test "Up" directed forces. The measurements of mechanical properties are collected 2 times per sample to confirm repeatability. Repeatability of the mechanical behavior is obtained for all samples evaluated.

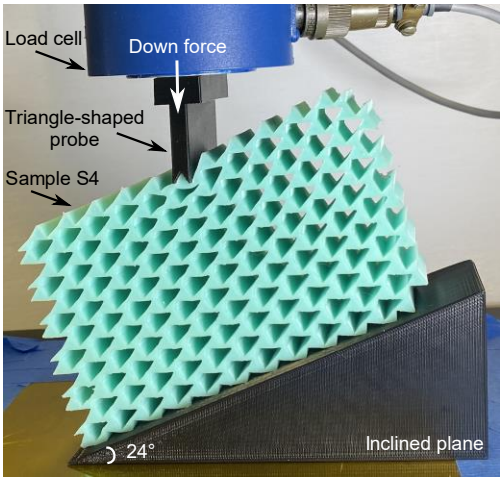

Figure S2. Experimental set-up for measurement of uniaxial mechanical properties, shown as an example for sample S4

1.3 Finite element modeling of mechanical properties

The finite element (FE) software COMSOL Multiphysics is used to predict the linear uniaxial mechanical properties and to confirm trends observed in the experimental characterization of mechanical properties.

The FE model boundary conditions correspond to experimental conditions where one side of the metamaterial sample is fixed, while the top center edge triangle on an opposite side of the sample displaces vertically. An isotropic linear elastic material model is employed with Young's modulus of 700 kPa, Poisson's ratio of 0.49, and density of 1145 kg/m^3. The material properties are derived from Ref. [1] that characterized the silicone rubber employed here. Minor discrepancies are observed between the measurements and model predictions in Figure 2(a) and (b) in the main text. The discrepancies may be associated with the partial displacement constraint in the experiments for the non-loaded sample side, so that small lateral sliding of the sample may occur. Yet, the salient trends and overall quantitative values measured experimentally remain similar to the FE model predictions.

1.4 Characterization of wave propagation

Digital image correlation is used to measure the dynamic behavior of the metamaterial samples subjected to impact at the same locations as those used for force application in the mechanical properties characterization. For high-speed video imaging, a speckle pattern is created on the metamaterial surface by randomly distributing carbon black microparticles (BOS Essential Activated Charcoal Powder) on the metamaterial surface. The metamaterial samples are placed on a flat plate. The top center edge triangle of metamaterial sample is struck with an impact hammer (PCB 086C03, Depew, NY). The same process is repeated for the opposite edge after rotating the sample by 180°. The images are recorded before and during deformation using a high-speed camera (Photron FastCam SA-X2) at an imaging rate of 20,000 frames per second. The experimental set-up is presented in Figure S3. Two LED lights (Neweer CN-216) are used to provide sufficient illumination for the recording. To post-process the high-speed video recordings, a MultiDIC open source toolbox for digital image correlation is used [2]. The MultiDIC takes advantage of the speckle pattern and correlates the subsets in the deformed image to the undeformed subset to provide the displacement magnitudes of sample during deformation. See corresponding videos in Supplemental Material, showing the propagation of waves in both metamaterial samples S2 and S3. The measurements of wave propagation induced by impact are collected multiple times per sample to confirm repeatability. Repeatability of the dynamic behavior is obtained for all samples evaluated.

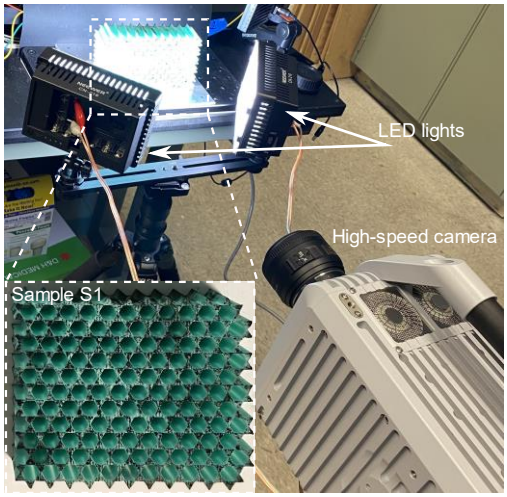

Figure S3. Experimental set-up to characterize propagation of elastic waves in metamaterial samples when subjected to impact. A speckled metamaterial sample S1, high-speed camera, and lighting apparatus are shown. The inset shows a detailed photograph of sample S1, speckled for the high-speed video recording.

2 Supporting results

The uniaxial mechanical stiffness values and polar elasticity coefficient PEC for metamaterial samples S1, S2, S3 and S4 are listed in Table S2. The qualitative trends between the experimental and simulation results are in agreement. It is observed that the PEC for the experimental samples S2, S3, and S4 are less than those computed via the simulations. The differences may be associated with the boundary conditions in the experiments that may permit small lateral motion on the bottom plate whereas the nominal boundary condition in the model is a fixed edge. The differences may also be due to minor inevitable imperfections in fabrication associated with the rubber casting process. Nevertheless, the agreement between simulated and experimental results indicates that the directional dependence in mechanical behavior predicted through the FE studies may be realized in the laboratory.

Table S2. Uniaxial mechanical stiffness values as well as polar elasticity coefficient PEC of metamaterial samples S1, S2, S3, and S4 determined by experiments and FE simulation.

Sample	Force	Uniaxial mechanical stiffness (N/mm)		Polar elasticity coefficient PEC	
		Experiment	Simulation	Experiment	Simulation
S1	Down Force	0.69	0.54	1.05	1.02
	Up Force	0.66	0.53		
S2	Down Force	0.20	0.31	0.38	0.60
	Up Force	0.52	0.52		
S3	Down Force	0.16	0.37	0.52	0.82
	Up Force	0.31	0.45		
S4	Down Force	0.43	0.42	1.08	2.00
	Up Force	0.40	0.21		

For the kagome lattice-based metamaterials studied in this research, axial (normal) and tangential (shear) stress components are coupled by the axial and bending deformations of the lattice unit cell geometries. This behavior, in turn, governs uniaxial mechanical stiffnesses observed at the metamaterial edges. As an example of such influences, Figure S4(a) presents simulation results of uniaxial mechanical properties of the opposite edges of metamaterial sample S2 as a function of oblique angle θ. Blue curves correspond to force applied downward from the top edge, while red curves correspond to force applied upward from the

bottom edge. The linear color gradients for the red and blue curves correspond to change in oblique angle θ from -90° to 90° by steps of 5° as the color gradation varies from the solid hue to light shading.

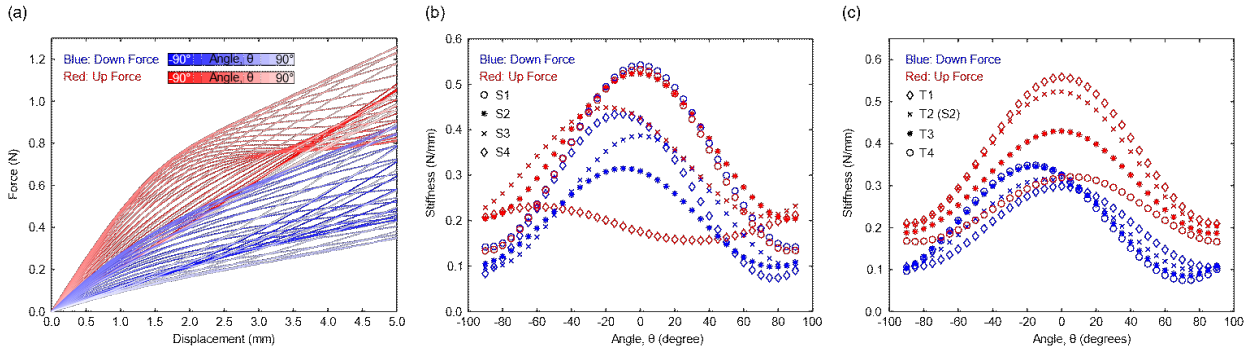

Figure S4. Finite-element simulation results of uniaxial mechanical properties of the opposite edges of metamaterial samples as a function of oblique angle θ. (a) Mechanical responses of metamaterial sample S2. (b) Uniaxial mechanical stiffnesses of regular (S1), deformed (S2), and twisted deformed (S3 and S4) kagome metamaterials. (c) Uniaxial mechanical stiffnesses of deformed kagome metamaterials T1, T2, T3, and T4, created with relative translations of the vertex of a unit cell triangle.

The slope of a line tangent to the mechanical properties characterization near the origin is considered to be the linear elastic, uniaxial mechanical stiffness of the metamaterial. Accordingly, Figs. S4(b) and (c) present the mechanical stiffnesses for the metamaterials considered in this work. As can be seen in Figs. S4(b) and (c), in general the minimum stiffness occurs when force is applied close to grazing incidence (θ = -90° and 90°). Sample S4 differs in this trend for upward directed force so that a minimum mechanical stiffness occurs around θ = 30°, Fig. S4(b). By contrast, the angle where the stiffness is maximum depends on the stress transfer mechanisms distinct to each metamaterial sample cross-section geometry. For example, as observed in Fig. S4(b) in the regular kagome lattice metamaterial sample S1 the maximum stiffnesses occur for normally applied force θ = 0°. For each deformed kagome lattice metamaterial samples S2, S3, and S4, the maximum stiffnesses occur for oblique force application angles that gradually deviate from normal incidence.

Fig. S4(c) compares the mechanical stiffnesses of the top and bottom edges for the deformed metamaterial samples T1, T2, T3, and T4 as a function of oblique angle. As the vertex of deformed unit cell triangle is shifted from symmetric conditions T1 to the cases of T2, T3, and T4, the maximum stiffness corresponding to downward directed force occurs for increasing oblique angle from θ = 0° to θ = -20°.

These findings demonstrate that the twisting and deformation of unit cell geometry governs the magnitude and orientation of peak mechanical stiffness exhibited by the metamaterial samples. On the other hand, the horizontal translation of one triangle node in the unit cell geometry primarily influences the oblique angle at which uniaxial mechanical stiffness is maximized when force is applied downward. The polar elasticity coefficient or PEC, presented in Figure 3 in the main text, is determined by calculating the ratio between the stiffness of the top and bottom edges (or Down Force/Up Force), obtained from Fig. S4.

3 Descriptions of supplemental videos

Video_S1. DIC results of displacement magnitudes of metamaterial sample S2 subjected to low-amplitude impact loading from opposite edges. In Video_S1 Left, the top center edge of metamaterial is struck with an input force of amplitude around 98 N and the video is played back at a rate of 1 s for 377 s of real-time. In Video_S1 Right, the bottom center edge of metamaterial is struck with an input force of amplitude around 94 N and the video is played back at a rate of 1 s for 687 s of real-time. Although the force applied on bottom edge is slightly less than the force applied on top edge, it is clear that from the bottom edge the shock wave propagates further inside the sample. This confirms that wave transmits more easily from the stiff edge (bottom edge of sample S2) while attenuates more from the floppy edge (top edge of sample S2). Also, the wave, starting from top edge, propagates more to the left directions, while the wave, starting from bottom edge, propagates more to the right direction. Overall, strong asymmetric edge wave transmission in topological sample S2 is found when struck from opposite edges.

Video_S2. DIC results of displacement magnitudes of metamaterial sample S2 subjected to high-amplitude impact loading from opposite edges. In Video_S2 Left, the top center edge of metamaterial is struck with an input force of amplitude around 217 N and the video is played back at a rate of 1 s for 317 s of real-time. In Video_S2 Right, the bottom center edge of metamaterial is struck with an input force of amplitude around 251 N and the video is played back at a rate of 1 s for 465 s of real-time. Unlike video S1, the force applied on bottom edge is higher than the force applied on top edge, and as a result, the wave propagation from the bottom (stiff) edge is significantly more than that of top (soft) edge. Accordingly, the asymmetric edge wave transmission between opposite edges becomes more pronounced.

Video_S3. DIC results of displacement magnitudes of metamaterial sample S3 subjected to low-amplitude impact loading from opposite edges. In Video_S3 Left, the top center edge of metamaterial is struck with an input force of amplitude around 85 N and the video is played back at a rate of 1 s for 348 s of real-time. In Video_S3 Right, the bottom center edge of metamaterial is struck with an input force of amplitude around 63 N and the video is played back at a rate of 1 s for 326 s of real-time. Similar to sample S2, although amplitude of the force applied on bottom edge is less than that of top edge, the shock wave propagates further from the bottom than top edge. The reason is that, again, in sample S3, the top edge is floppy which causes more attenuation of shock waves and bottom edge is stiff, leading to more wave propagation. Also, the wave, propagates more to the left directions if top edge is struck, while the wave propagates more to the right direction if the bottom edge is struck.

Video_S4. DIC results of displacement magnitudes of metamaterial sample S3 subjected to high-amplitude impact loading from opposite edges. In Video_S4 Left, the top center edge of metamaterial is struck with an input force of amplitude around 145 N and the video is played back at a rate of 1 s for 336 s of real-time. In Video_S4 Right, the bottom center edge of metamaterial is struck with an input force of amplitude around 159 N and the video is played back at a rate of 1 s for 434 s of real-time. At a higher applied force from bottom edge than that of top edge, the wave propagation from the bottom (stiff) edge is significantly more than that of top (soft) edge and thus, the asymmetric edge wave transmission between opposite edges becomes more pronounced.

References

[1] S. Cui and R.L. Harne, Characterizing the nonlinear response of elastomeric material systems under critical point constraints, International Journal of Solids and Structures **135**, 197-207 (2018).

[2] D. Solav, K.M. Moerman, A.M. Jaeger, K. Genovese, and H.M. Herr, MultiDIC: An open-source toolbox for multi-view 3D digital image correlation, IEEE Access **6**, 30520-30535 (2018).